.

Reconstruction and identification of electrons and photons with the ATLAS detector at the LHC

Valentina Gallo
On behalf of the ATLAS Collaboration

Albert Einstein Center for Fundamental Physics
Laboratory for High Energy Physics (LHEP), University of Bern
Sidlerstrasse 5, CH-3012 Bern
Switzerland

ATL-PHYS-PROC-2012-044
21 February 2012

ABSTRACT

Measurements of electron and photon reconstruction and identification performance with the ATLAS detector at the Large Hadron Collider (LHC) are reported. The results are based on studies of Z, W and J/Ψ decays and diphoton production, collected in proton-proton collisions at a centre-of-mass energy of 7 TeV. Most of the measurements use an integrated luminosity of 40 pb^{-1} recorded in 2010. The determination of the photon pointing resolution of the EM calorimeter was performed with an integrated luminosity of 1 fb^{-1}.

Introduction

The precise reconstruction and efficient identification of electrons and photons at the Large Hadron Collider (LHC) is essential for a large variety of physics analyses, including Standard Model (SM) precision measurements, searches for Higgs bosons (e.g. $H \to \gamma\gamma$) and new phenomena beyond the Standard Model (e.g. $Z' \to ee$). The ATLAS detector was designed to have excellent performance for electrons and photons from a few GeV up to several TeV. The processes of interest often have a low cross section and are covered by large backgrounds from SM events with hadronic jets. Therefore high reconstruction and identification efficiency and large jet rejection are necessary. In the following, after a brief description of the ATLAS detector, the electron and photon reconstruction algorithms are outlined. The photon pointing resolution and the in-situ electron energy calibration are then discussed. Finally, the electron and photon

identification methods and their efficiencies measured in the 2010 dataset are presented.

1 The ATLAS detector

The ATLAS detector is composed of several sub-detectors, here just those needed for the electron and photon identification are described. A full description of the ATLAS detector can be found in Ref. [1].

The coordinate system used by ATLAS is a right-handed system with the z axis defined by the beam direction. The direction from the interaction point, placed in the center of the ATLAS detector, to the center of the LHC ring defines the positive x axis. The y axis points upward from the zx plane. The polar angle θ is the angle from the z axis and the pseudorapidity is defined as $\eta = -ln\tan(\theta/2)$. The azimuthal angle ϕ is measured around the beam axis.

Charged particle tracks are reconstructed in the Inner Detector (ID) within a pseudorapidity range of $|\eta| < 2.5$. The ID is placed close to the beam pipe and is immersed in a 2 T magnetic field generated by a solenoid. It is made of three sub-detectors. The pixel detector consisting of three layers is the closest to the beam pipe; four layers of stereo pairs of silicon microstrips (SCT) provide eight hits per track at intermediate radius; the transition radiation tracker (TRT) made of layers of gaseous straw tubes provides about 35 hits per track.

The electromagnetic (EM) calorimeter is made of lead-liquid argon detectors with an accordion shape geometry that provides a full ϕ coverage without any cracks. The EM calorimeter is divided into three layers: *strip*, *middle* and *back*. Along η, the central part of the calorimeter is composed of two half-barrels, centered around the z axis and covering a pseudorapidity range of $|\eta| < 1.47$. The outer part of the EM calorimeter is made of two wheels on each side of the electromagnetic barrel. The inner (EMEC-IW) and the outer (EMEC-OW) end-cap wheels cover the ranges of $1.375 < |\eta| < 2.5$ and $2.5 < |\eta| < 3.2$, respectively. The transition region between the barrel and the end-cap calorimeters ($1.37 < |\eta| < 1.52$) has a large amount of inactive material in front of the first active calorimeter layer, therefore it is expected to contribute with poorer performance. Most of the EM shower energy for high energy particles is collected in the middle layer that has a granularity of $\eta \times \phi = 0.025 \times 0.025$. The first strip layer provides a good $\gamma - \pi^0$ discrimination thanks to its finer-grained strips along η with a coarser granularity in ϕ (for instance $\Delta\eta \times \Delta\phi = 0.003 \times 0.1$ in the barrel). The back layer collects the energy deposits from very high energy EM showers. In addition, a presampler detector with a coverage of $|\eta| < 1.8$ is placed in front of the EM calorimeter in order to correct for the energy lost in the material in front of the EM calorimeter.

Surrounding the EM calorimeter there are the hadronic calorimeters that are used in the context of this note for electrons and photons identification.

2 Electron and photon reconstruction

The electron and photon reconstruction [2, 3] in the central region of the calorimeter system ($|\eta| < 2.47$) starts with the evaluation of the energy deposits in clusters. A sliding window algorithm searches for clusters of longitudinal towers

with total transverse energy above 2.5 GeV. The window size is 3×5 in middle layer cell units ($\eta \times \phi = 0.025 \times 0.025$). Afterwards, the matching of a track with an EM cluster is made by extrapolating from the last measurement point to the middle layer cluster of the EM calorimeter. The distance between the track and the cluster position has to be less than 0.05 along η and 0.1 along ϕ to take into account for bremsstrahlung losses. In case of multiple tracks matching the same cluster, tracks with hits in the silicon detectors are preferred and the closest in terms of $\Delta R = \sqrt{\Delta\eta^2 + \Delta\phi^2}$ is chosen.

The photons are identified as unconverted if the cluster does not match any track in the ID, while electrons are selected when at least one track can be associated to the reconstructed cluster. To recover photons that have converted into an electron pair, the cluster is required to match pairs of tracks originating from a reconstructed conversion vertex. Moreover, to increase the reconstruction efficiency, converted photons with only one track (due to a misreconstruction of the second) are also retained in case the track does not have any hits in the innermost layer of the pixel detector. EM clusters are then rebuilt in an optimized cluster size of $\Delta\eta \times \Delta\phi = 3 \times 7$, in middle layer cell units, for electrons and converted photons in the barrel. The size along ϕ is enlarged to account for the Bremsstrahlung losses and to compensate for the bending due to the tracker magnetic field. For unconverted photons the cluster size in the barrel is $\Delta\eta \times \Delta\phi = 3 \times 5$. In the end-cap, a cluster size of 5×5 is used for all objects. The energy of electrons and photons is computed by a weighted sum of four different contributions in the EM calorimeter system [4]: the energy deposit in the material in front of the EM calorimeter; the energy deposit in the cluster; the external energy deposit outside the cluster (lateral leakage) and the energy deposit beyond the EM calorimeter (longitudinal leakage).

In the *forward* region ($2.5 < |\eta| < 4.9$) only information from the calorimeters can be used, since the tracking system is limited to $|\eta| < 2.5$. Therefore, the selection of electrons relies only on the energy deposit in the calorimeter cells. In particular, shower shapes provide efficient identification thanks to good transverse and longitudinal segmentation of the calorimeters.

The four-momentum for electrons within $|\eta| < 2.5$ is computed using informations both from the reconstructed cluster and the best matched track. The energy is given by the cluster energy and the ϕ and η directions are taken from the corresponding track parameters at the vertex. In absence of tracks, as in the case of photons, the direction is taken using the information from the calorimeter as it is described in section 2.1. A dedicated energy calibration is also applied as outlined in section 2.2.

2.1 Pointing resolution

In processes such as $H \to \gamma\gamma$, the angle between the two photons is needed for the computation of the diphoton mass. This angle is determined from the interaction vertex position and the photon impact points in the calorimeter. The resolution of this angle is dominated by the reconstruction of the primary vertex z position. The RMS vertex spread in the z direction is around 5.5 cm. The event by event interaction vertex can be determined more accurately. If neither of the photons convert to electron positron pairs, the vertex reconstruction has to rely on information provided by the calorimeter since there are no tracks. The photon direction in this case is computed using the first and second layer of the

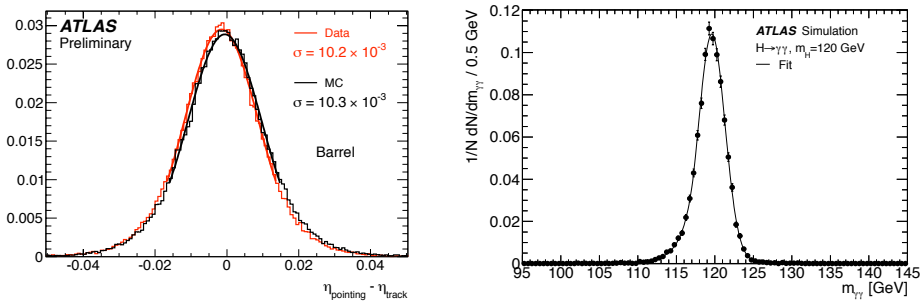

Figure 1: (Left) Comparison between the η measurements of the calorimeter pointing and the more precise inner detector tracking in $Z \to ee$ decays in the barrel region [5]. Data (red) are compared to simulation (black). (Right) The reconstructed diphoton invariant mass distribution of a simulated Higgs boson signal with a mass of 120 GeV [6].

EM calorimeter. The vertex is reconstructed from the photon directions and the resolution is about 1.6 cm in z. For converted photons with tracks, the vertex position is estimated also taking in account the conversion vertices from both photons and combined with the average beam spot in z. Here the resolution is better. This method has been tested using $Z \to ee$ decays as a control sample. As shown on the left side of Figure 1, the data agree well with the Monte Carlo prediction. The resulting impact of the angle measurement on the invariant mass resolution is negligible compared to the contribution from the photon energy resolution. The mass resolution is 1.4 GeV for unconverted photons both belonging to the central part of the calorimeter ($|\eta| < 0.75$). This value increases to 2.1 GeV if at least one photon is converted and at least one photon is near the transition between the barrel and the end-cap ($1.3 < |\eta| < 1.75$). In this case, the energy resolution is degraded because the large amount of material in front of the EM calorimeter that affects, in particular, converted photons. On the right side of the figure, an example of mass resolution for an hypothetic 120 GeV mass Higgs boson is shown for all photon categories (i.e. from several combination of photon pairs involving converted and unconverted photons interacting in the EM calorimeter). The diphoton mass has been fitted with a Crystal Ball function convoluted with a Gaussian and the resulting mass resolution is 1.7 GeV [6].

2.2 In situ calibration

The energy scale of the incident electron has been evaluated in situ profiting from the well known mass of the Z boson. The measurements reported in the following have been obtained with the data collected in 2010, corresponding to an integrated luminosity of about 40 pb^{-1}. A complete description can be found in Ref. [7]. The method consist of constraining the invariant mass distribution of electron-positron pairs from Z decays to the known Z line shape in order to evaluate the residual miscalibration. Therefore, the the energy measured by the calorimeter ($E^{\rm meas}$) is parametrized as $E^{\rm meas} = E^{\rm true}(1+\alpha)$, where $E^{\rm true}$ is the

.

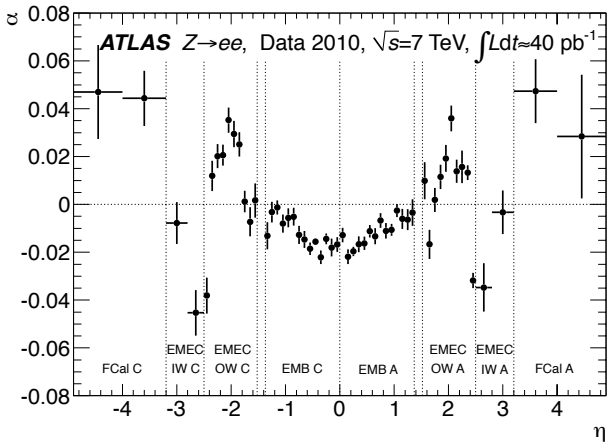

Figure 2: The energy scale correction as a function of the pseudorapidity of the electron cluster derived from Z decays [7]. The uncertainties are statistical only.

true electron energy and α is the residual miscalibration. In Figure 2 the value of α as a function of pseudorapidity is shown. The α values are within $\pm 2\%$ in the barrel and grow up to $\pm 5\%$ in the forward region. The rapid change at some η values is dictated by the transition between different EM calorimeter components as shown in Figure 2. The variation within a given calorimeter component are due to several effects related to electronic calibration, high voltage correction, additional material in front of the calorimeter, differences in the calorimeter and presampler energy scales, and differences in lateral leakage between data and Monte Carlo. Complementary in-situ calibration methods have also been considered in order to validate the baseline calibration. One way is to use the same method as for $Z \to ee$ decays, but for $J/\Psi \to ee$ decays. Another one is to constrain the energy measurement E in the EM calorimeter to the momentum measurement p of electrons in the ID. As the mass of the electron can be neglected, the ratio E/p should, in absence of detector effects and bremsstrahlung, be unity. The methods are complementary as they use different datasets and rely on different observables.

After the baseline energy scale correction using $Z \to ee$ decays, the α values have been evaluated with these two alternative methods and they agree with unity within the measurement errors. On the left side of Figure 3, the α values as a function of the pseudorapidity are shown for $J/\Psi \to ee$ decays. On the right side of the figure, the same distribution is shown but for the $W \to e\nu$ decays. These results demonstrate that the energy calibration corrections obtained from $J/\Psi \to ee$ and $W \to e\nu$ decays agree well with the baseline method using $Z \to ee$ decays.

The energy scale α has been determined with a precision of $0.3\% - 1.6\%$ in bins of η in the central part ($|\eta| < 2.47$) of the EM calorimeter. In the forward region the uncertainty increases up to $2\% - 3\%$.

The fractional energy resolution σ_E/E in the calorimeter is parametrized by

.

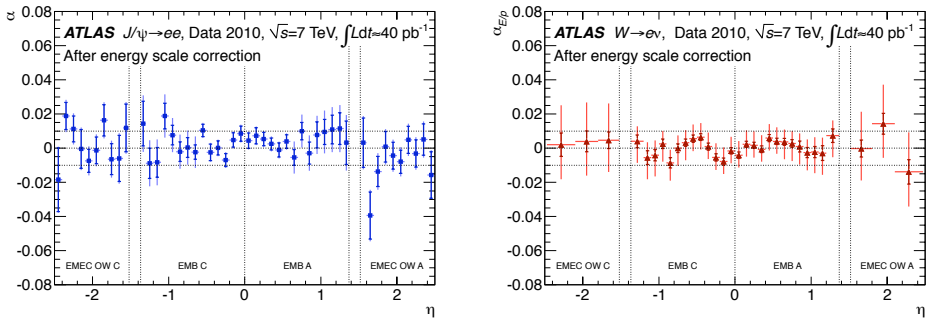

Figure 3: Energy scale values for $J/\Psi \to ee$ and $W \to e\nu$ decays as a function of the pseudorapidity η [7]. On the left the energy scale values are obtained using the dielectron mass from $J/\Psi \to ee$ decays. On the right the results from the E/p method using $W \to e\nu$ decays are shown. The results are given with the statistical (inner bars) and total (outer bars) errors.

the formula:

$$\frac{\sigma_E}{E} = \frac{a}{\sqrt{E}} \oplus \frac{b}{E} \oplus c$$

where a is the sampling term, b is the noise term and c is the constant term. The construction tolerances and the calibration system ensure that the response is locally uniform within 0.5% over regions of size $\Delta\eta \times \Delta\phi = 0.2 \times 0.4$ in the EM calorimeter [8]. These regions are expected to be inter-calibrated in situ to 0.5%, achieving a global constant term of about 0.7% [9].

At low energy, the energy resolution is expected to be dominated by the contribution from the sampling term a and thus J/Ψ events are used here. As shown on the left side of Figure 4, the dielectron mass of $J/\Psi \to ee$ decays is well described by the MC for both the mean and the width. Therefore, it is assumed that the sampling term is well described by the MC within a 10% uncertainty.

The noise term also contributes significantly only at low energy. However, the noise description in the MC simulation is derived from calibration data runs. Therefore, its effect on the measurement of the constant term cancels out to first order.

The effective constant term c_{data} can be described by:

$$c_{\text{data}} = \sqrt{2 \cdot \left(\left(\frac{\sigma}{m_Z} \right)_{\text{data}} - \left(\frac{\sigma}{m_Z} \right)_{\text{MC}} \right) + c_{\text{MC}}^2}$$

where c_{MC} is the constant term of about 0.5% in the MC simulation, m_Z indicates the Z mass [10] and σ the gaussian component of the experimental resolution. The resulting effective constant term, which includes both the calorimeter constant term and the effect of inhomogeneities due to possible additional material, has been measured using the dielectron mass of $Z \to ee$ decays. An example of the dielectron mass distribution is shown on the right side of Figure 4, when both electrons are reconstructed within $|\eta| < 2.47$. The effective constant term

.

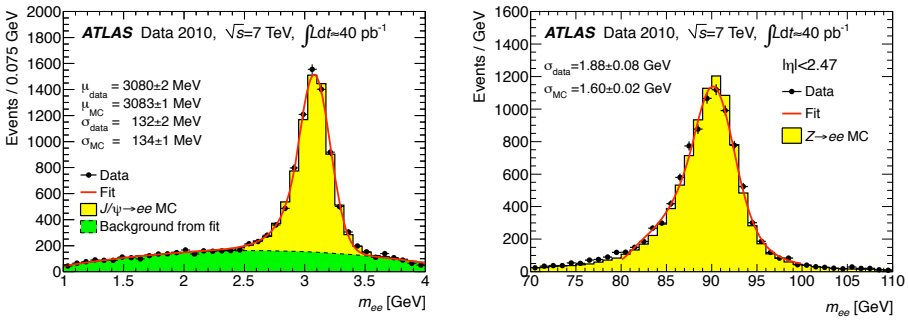

Figure 4: (Left) Reconstructed dielectron mass distribution for $J/\Psi \rightarrow ee$ decays after applying the scale factor corrections [7]. The data (full circle) are compared to the MC signal (yellow filled area). The background contribution (green area) is described by a Chebyshev polynomial. The mean (μ) and the width (σ) of the fitted Crystal Ball function are given for both data and MC. (Right) The reconstructed dielectron mass distribution for $Z \rightarrow ee$ decays after applying the calibration when both electron and positron are reconstructed within $|\eta| < 2.47$ [7]. The data (full circle) are shown together with the statistical error bars and they are compared to the signal Monte Carlo expectation (filled yellow area). The fit function is a Breit-Wigner convoluted with a Crystal Ball function and is shown in red. The data and Monte Carlo widths (σ) of the Gaussian of the Crystal Ball are shown.

is measured to be $(1.2 \pm 0.1(\text{stat})^{+0.5}_{-0.6}(\text{syst}))\%$ in the barrel ($|\eta| < 1.37$). In the end cap the effective constant term grows up to 1.8%, and reaches about 3% in the forward region.

Thanks to the larger amount of data collected in 2011 an improvement of the energy scale determination in (η , ϕ) bins is expected together with a better knowledge of the material in front of the detector.

3 Electron and photon identification

The baseline electron and photon identification relies on a cut based selection. A complete list of variables used for the baseline electron and photon selection and a treatment of the expected performance can be found in [2, 3]. In the following the main aspects of the selections are described.

For electrons, three sets of cuts have been developed (*loose*, *medium* and *tight*) with increasing jet rejection power. The method relies on information from both the calorimeter and the tracking system to suppress hadrons misreconstructed as electrons and to discriminate against photon conversions.

Two sets of selections have been developed for photons (*loose* and *tight*). The selections depend on cuts using calorimeter variables which provide a good identification of signal photons and a good discrimination from fake signatures due to QCD multi-jets events. The calorimeter variables used for both electrons and photons can be grouped in: hadronic leakage variables measuring the energy deposit in the hadronic calorimeter, variables using the middle layer of the

EM calorimeter and variables using the strip layer. Moreover, combined informations from the track and the cluster, such as the track-cluster matching in η and ϕ and the E/p ratio, are used for the electron identification. In section 3.1 the resulting identification efficiency both for electrons and photons are shown.

3.1 Identification efficiency

Efficiency measurements for both electrons and photons have been performed with the data collected in 2010.

The efficiencies for two of the electrons identification selections (*medium* and *tight*) have been evaluated using the tag and probe method on $Z \to ee$, $W \to e\nu$ and $J/\Psi \to ee$ envents, in order to cover a wide range of energy and perform a crosscheck with different processes. The method consists of selecting a set of dielectron events where one of the electron (*tag*) passes a tight selection. The second electron (*probe*) is required to pass only minimal requirements on the number of silicon hits. The efficiency is defined by the fraction of *probe* electrons passing the final selection criteria. For $W \to e\nu$ decays, high missing transverse momentum is used as *tag*. This method has been used also for other measurements, in particular the reconstruction and the trigger efficiency, and the charge misidentification rate. Here only selected results from the identification efficiency measurements are discussed. More details can be found in Ref. [7].

In the central region of the calorimeter ($|\eta| < 2.47$) a precise measurement of the identification efficiency has been performed both as a function of η and E_T, in the electron transverse energy range $E_T = 4-50$ GeV. On the top of Figure 5 the resulting efficiency for *medium* (left) and *tight* (right) selections are shown as function of E_T when the tag and probe method is applied to $Z \to ee$ decays. The same selection has been applied to the Monte Carlo for comparison, as shown in the figure. On the bottom plots of Figure 5 the identification efficiencies as a function of the pseudorapidity are shown for *medium* (left) and *tight* (right) selections.

The identification efficiency has been measured also at low transverse energy range (below 20 GeV) using $J/\Psi \to ee$ decays as shown in Figure 6. The measurement has been performed in an integrated η range due to the limited statistics. The measured efficiency has been compared with a weighted average of the efficiency expected from prompt $pp \to J/\Psi + X$ and non prompt $bb \to J/\Psi + X$ production. Leptons coming from non prompt decays are typically less isolated and therefore fail at higher rate the electron identification criteria. The measured efficiency is compatible with the MC prediction within the uncertainty as shown in Figure 6.

In summary the electron identification efficiency has been measured over an energy range of 20 GeV $< E_T <$ 50 GeV with $W \to e\nu$ and $Z \to ee$ decays. The resulting efficiency is above 90% (around 80%) for *medium* (*tight*) selection. At lower energy (4 GeV $< E_T <$ 20 GeV) the efficiency has been measured using $J/\Psi \to ee$ decays and cross checked (for 15 GeV $< E_T <$ 20 GeV) with $W \to e\nu$ decays. It is above 75% for *medium* selection and above 60% for *tight*.

As opposed to the electron measurements, the method performed to measure the identification efficiency for photons is not completely data driven. The difficulty is due to the absence of a clear signature for a tag and probe method at high photon energy. The identification efficiency measurements for photons have been conducted in the context of the diphoton cross section measurement [11].

.

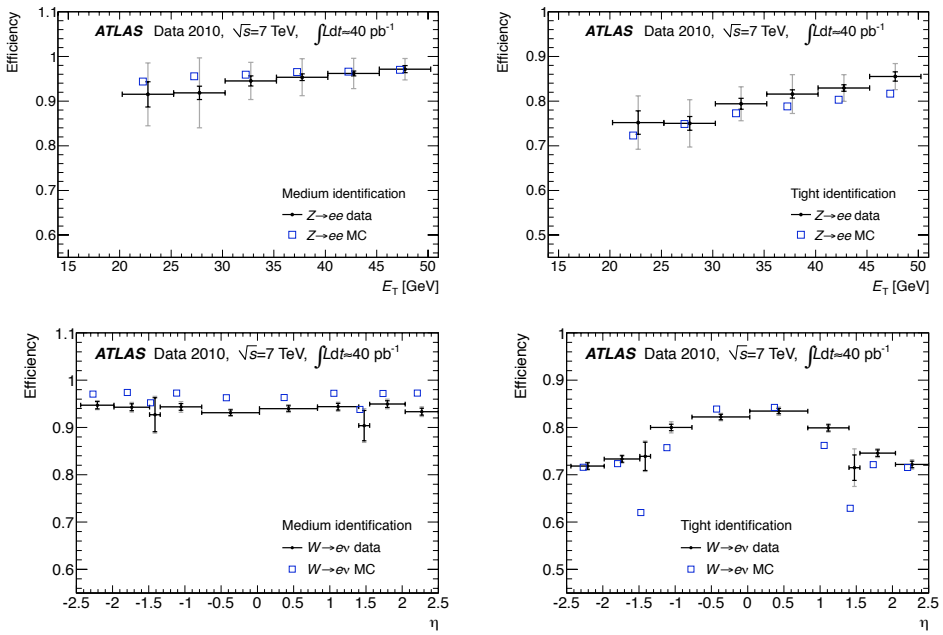

Figure 5: Identification efficiency measured using $Z \to ee$ and $W \to e\nu$ decays [7]. On the top, the efficiency is shown as a function of the transverse momentum, integrated over all $|\eta| < 2.47$ (excluding $1.37 < |eta| < 1.52$) for *medium* (left) and *tight* (right) selections. On the bottom, the peseudorapidity dependence is presented for electrons with $20 < E_T < 50$ GeV. The results obtained with data are shown with the full circle with statistical (inner bars) and total (outer bars) uncertainties. The Monte Carlo estimates are also shown (blue empty squares). The statistical uncertainty is negligible.

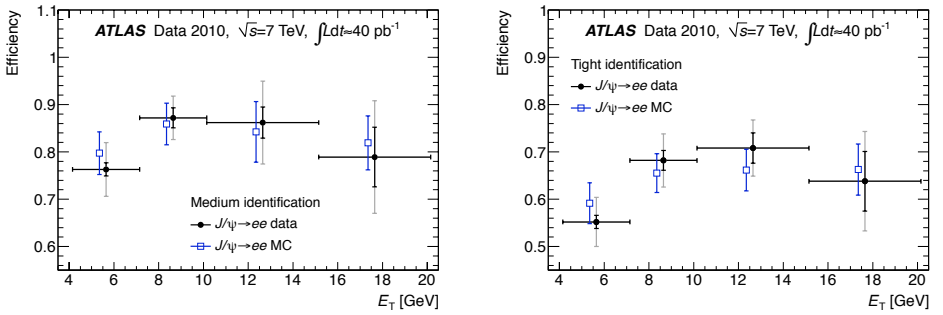

Figure 6: Identification efficiencies measured using $J/\Psi \to ee$ decays [7]. The efficiency is shown as a function of E_T integrated over all $|\eta| < 2.47$ (excluding $1.37 < |eta| < 1.52$), for *medium* (left) and *tight* (right) selections. The black full circles describe the data measurements with the statistical (inner bars) and total (outer bars) uncertainties. The MC prediction with its total uncertainty is also shown (empty blue squares).

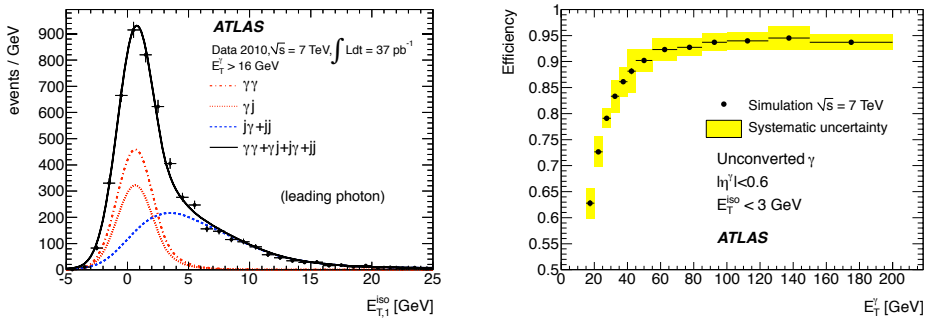

Figure 7: (Left) The isolation (E_T^{iso}) distribution for the leading photon in diphoton events when both photons satisfy the *tight* selection criteria [11]. The solid circle points represent the data, the black solid line indicates the resulting fit, while the dash-dotted curves show the diphoton component. The blue dashed line represents the background component. (Right) Tight photon identification efficiency as a function of the reconstructed photon transverse energy for unconverted photons for $|\eta| < 0.6$ [5]. The efficiency is calculated with respect to reconstructed true photons satisfying $E_T^{iso} < 3$ GeV. The yellow bands include the systematic uncertainties.

An important isolation requirement to select prompt photons is based on the transverse energy deposit in the calorimeter within a cone around the photon candidate. On the left side of Figure 7, the distribution of the transverse isolation energy (E_T^{iso}) is shown for the leading photon passing the *tight* selection. The E_T^{iso} is defined as the sum of the energies in the cells of the electromagnetic and hadronic calorimeters excluding the contribution from the 5×7 EM calorimeter cells in the $\eta - \phi$ plane. The E_T^{iso} is corrected for the photon leakage and the ambient energy density measured in the event. The efficiency is determined by applying the identification criteria to a Monte Carlo photon sample where the photon shower shape variables have been shifted with correction factors that take into account the observed average differences between the discriminating variables in data and in Monte Carlo. A cut on the E_T^{iso} is performed in order to isolate the prompt component ($E_T^{iso} < 3$ GeV). The efficiency of the *tight* identification for true reconstructed photons passing the isolation requirements is shown on the right hand side of Figure 7. It has been evaluated as a function of η and the photon transverse energy E_T. Here only one η region is shown. The identification efficiency is defined as the ratio between the number of reconstructed photons passing the identification criteria and the number of reconstructed true photons with $E_T^{iso} < 3$ GeV.

The resulting efficiency is η dependent and increases with the transverse energy, going from 60% at low E_T (16 GeV $< E_T <$ 20 GeV) up to more then 90% for $E_T > 100$ GeV.

4 Conclusion

Electron and photon reconstruction and identification have been studied with data collected in 2010 proton-proton collisions at a centre-of-mass energy of $\sqrt{s} = 7$ TeV.

The electron energy scale of the EM calorimeter has been determined with a precision of $0.3\% - 1.6\%$ in bins of η in the central part of the EM calorimeter ($|\eta| < 2.47$). In the forward region the uncertainty on the energy scale increases up to $2\% - 3\%$. After applying the energy scale correction factors, the effective constant term of the energy resolution is measured to be $(1.2 \pm 0.1(\text{stat})^{+0.5}_{-0.6}(\text{syst}))\%$ in the barrel ($|\eta| < 1.37$). The effective constant term increases up to 1.8% in the end-cap and reaches about 3% in the forward region.

The calorimeter pointing resolution has also been evaluated. This important method provides an improvement of the $H \to \gamma\gamma$ measurement performance especially in high pileup condition. The resulting impact of the angle measurement on the invariant mass resolution is negligible compared to the contribution from the photon energy resolution. The mass resolution is 1.7 GeV for a simulated 120 GeV mass Higgs boson signal.

Moreover, the identification efficiency for both electrons and photons has been evaluated, with a data driven method for the electrons. For electrons with 20 GeV $< E_T <$ 50 GeV the resulting efficiency is above 90% and around 80% for *medium* and *tight* selection, respectively. At lower energy (4 GeV $< E_T <$ 20 GeV) the efficiency is above 75% for *medium* selection and above 60% for *tight*. In general the agreement between data and Monte Carlo is good. Photons are identified with an efficiency going from 60% at low E_T (16 GeV $< E_T <$ 20 GeV) to more then 90% for $E_T >$ 100 GeV. Already with the limited amount of the 2010 data, precise measurements of electron and photon performance have been obtained. More precise measurements in terms of a refined (η, ϕ) granularity and a better estimation of the constant term are expected with more than 5 fb^{-1} of integrated luminosity collected by ATLAS in 2011.

References

[1] ATLAS Collaboration, *The ATLAS Experiment at the CERN Large Hadron Collider*, JINST **3** (2008) S08003.

[2] ATLAS Collaboration, *Expected electron performance in the ATLAS experiment*, ATL-PHYS-PUB-2011-006.
https://cdsweb.cern.ch/record/1345327?ln=en

[3] ATLAS Collaboration, *Expected photon performance in the ATLAS experiment*, ATL-PHYS-PUB-2011-007.
https://cdsweb.cern.ch/record/1345329?ln=en

[4] ATLAS Collaboration, *Expected performance of the ATLAS experiment: detector, trigger and physics*, CERN-OPEN-2008-20, arXiv:0901.0512 [hep-ex].

[5] https://twiki.cern.ch/twiki/bin/view/AtlasPublic

[6] ATLAS Collaboration, *Search for the Standard Model Higgs boson in the two photon decay channel with the ATLAS detector at the LHC*, Phys.Lett.B **705** (2011) 452-470, arXiv:1108:5895 [hep-ex].

[7] ATLAS Collaboration, *Electron performace measurements with the ATLAS detector using the 2010 LHC proton-proton collision data*, submitted to Eur. Phys. J. C, arXiv:1110.3174 [hep-ex].

[8] J. Colas et al., *Response Uniformity of the ATLAS Liquid Argon Electromagnetic Calorimeter*, Nucl.Instrum.Meth. **A582** (2007) 429-455, arXiv:0709.1094 [physics.ins-det].

[9] ATLAS Collaboration, *ATLAS detector and physics performance: Technical Design Report, Vol. 1.*, Technical Design Report ATLAS. CERN, Geneva, 1999 CERN/LHCC 99-14 ATLAS TDR 14.
https://cdsweb.cern.ch/record/391176?ln=en

[10] The ALEPH, DELPHI, L3, OPAL and SLD Collaborations, *Precision electroweak measurements on the Z resonance*, Physics Reports **427** (2006) 257-454, arXiv:hep-ex/0509008.

[11] ATLAS Collaboration, *Measurement of the isolated diphoton cross section in pp collisions at* $\sqrt{s} = 7$ *TeV with the ATLAS detector*, Phys. Rev. **D85** (2012) 012003, arXiv:1107.0581 [hep-ex].